Monthly Notices of the ROYAL ASTRONOMICAL SOCIETY

MNRAS **488,** 224–233 (2019) doi:10.1093/mnras/stz1683
Advance Access publication 2019 June 19

On the radio image of relativistic jets – I. Internal structure, Doppler boosting, and polarization maps

A. V. Chernoglazov,[1,2,3★] V. S. Beskin[2,3] and V. I. Pariev[2]

[1] *University of New Hampshire, 105 Main St, Durham, NH 03824, USA*
[2] *P.N. Lebedev Physical Institute, Leninsky Prospekt 53, Moscow 119991, Russia*
[3] *Moscow Institute of Physics and Technology, Institutsky Per. 9, Dolgoprudny, Moscow Region 141700, Russia*

Accepted 2019 June 8. Received 2019 May 14; in original form 2018 September 5

ABSTRACT

In this first paper from forthcoming series of works devoted to radio image of relativistic jets from active galactic nuclei the role of internal structure of a flow is discussed. We determine the radial profiles of all physical values for reasonable Michel magnetization parameter $\sigma_{\rm M}$ and ambient pressure $P_{\rm ext}$. Maps of Doppler boosting factor δ and observed directions of linear polarization of synchrotron emission are also constructed.

Key words: galaxies: active – galaxies: jets – radiation mechanisms: non-thermal.

1 INTRODUCTION

Recent progress in high angular resolution very long baseline interferometry (VLBI) observations of relativistic jets outflowing from active galactic nuclei (AGNs; Mertens et al. 2016; Pushkarev et al. 2017) allows us to investigate directly their internal structure. In particular, the observations give us direct information about the dependence of the jet width $r_{\rm jet}(l)$ on the distance l from the 'central engine'.

Progress in VLBI observations allows us also to relate to more detailed information from the theory of relativistic jets. In spite of the wide variety of analytical and numerical models on jets acceleration and confinement (Vlahakis & Königl 2003; McKinney 2006; Komissarov et al. 2007; Tchekhovskoy, Narayan & McKinney 2011; McKinney, Tchekhovskoy & Blandford 2012; Potter & Cotter 2015) considering different solutions for jets shapes, there is no common point of view on the internal structure of relativistic jets.

In a number of works (Pariev, Istomin & Beresnyak 2003; Lyutikov, Pariev & Gabuzda 2005; Porth et al. 2011; Fendt, Porth & Sheikhnezami 2014) observable maps of synchrotron polarization and Faraday rotation for different models of relativistic jets in AGNs are suggested. The distribution of these quantities contains the information about magnetic field geometry, which is mostly toroidal. On the other hand, no predictions about Doppler boosting factor distribution have been done. The Doppler boosting factor was present in formulas, but its importance was not analysed. The ignorance of the Doppler boosting factor map was based on smallness of variation of toroidal velocity component ($v_\varphi \ll c$), and it used to be impossible to measure the velocity directly. Nevertheless, it has been recently discovered (Mertens et al. 2016) via wavelet analysis that the radiating plasma inside the jet in the nearest radio galaxy M87 rotates slowly.

Another vital difference of our consideration from previous ones is the ability to consider all parts of the jet self-consistently. Below we use our model of quasi-cylindrical flow with zero total electric current inside the jet submerged into warm external gas at rest with reasonable thermal pressure: we do not assume either external uniform magnetic field or electromagnetic discontinuities at the jet boundary that were appearing in many works (see e.g. Lyubarsky 2009; Martí 2015). This model gives us possibility to construct the most comprehensive radio map of Fanaroff–Riley II (FRII)-type jet.

The problem of the pressure-balanced jet without current sheet was considered by Gourgouliatos et al. (2012) (see also Kim et al. 2017, 2018). But their consideration was based on modification of Lundquist (1950) force-free solution, where the gas pressure was not related to density by a reasonable equation of state (the same approximation was used by Martí 2015). In addition, it was assumed that the toroidal component of magnetic field is of the same order as the poloidal one $B_z \sim B_\varphi$ instead of $B_z \ll B_\varphi$ in our model.

This paper is the first one in the forthcoming series of works where we will investigate the footprints of internal structure of relativistic jets in their radio images. For this we determine the transverse profiles of main physical parameters of relativistic jets such as the number density of particles, $n_{\rm e}$, and toroidal and poloidal components of velocity $\boldsymbol{v}$ and magnetic field $\boldsymbol{sB}$. Below we use semi-analytical 1D cylindrical approach introduced by Beskin (1997) and Beskin & Malyshkin (2000). Further researches (Lery et al. 1999; Beskin & Nokhrina 2006, 2009; Lyubarsky 2009; Nokhrina et al. 2015) demonstrated that this simple approach allows us to describe principal properties of the internal structure of relativistic jets. For example, analytical asymptotic solutions for hydrodynamical Lorentz factor γ,

$$\gamma \approx \frac{r_\perp}{R_{\rm L}}, \qquad R_{\rm c} > \frac{r_\perp^3}{R_{\rm L}^2}, \tag{1}$$

★ E-mail: chernoglazov_aleksandr@mail.ru

$$\gamma \approx \left(\frac{R_{\rm c}}{r_{\perp}}\right)^{1/2}, \qquad R_{\rm c} < \frac{r_{\perp}^3}{R_{\rm L}^2}, \tag{2}$$

which was later reproduced numerically in 3D simulations (McKinney 2006; Komissarov et al. 2007; Tchekhovskoy et al. 2011). Here $r_{\perp}$ is the distance from the rotation axis, $R_{\rm L} = \Omega/c$ is the radius of the light cylinder, and $R_{\rm c}$ is the curvature radius of magnetic surface.

In the first paper of the series of works we present maps (two-dimensional distributions) of the Doppler boosting factor,

$$\delta = \frac{\sqrt{1 - v^2/c^2}}{1 - v\cos\chi/c}, \tag{3}$$

and unit vector of the wave electric field in linearly polarized synchrotron radiation on the circular cross-sections of the jet. In expression (3) χ is the angle between the velocity of a parcel of plasma and the line of sight. These maps are determined by the magnetic field and the velocity of the magnetohydrodynamics (MHD) flow in the jet only, and are not influenced by the distribution of the number density of relativistic emitting particles, which is a major unknown ingredient in the jet models. More detailed simulations of observable radio images of jets on the sky, including the impact of the modelling of radiating particles distributions and spectra, will be presented in the forthcoming paper.

2 1D CYLINDRICAL GRAD–SHAFRANOV EQUATION

Basic equations describing the structure of relativistic axisymmetric stationary flows within Grad–Shafranov approach were formulated about 40 yr ago (e.g. see Ardavan 1976). This approach allows us to determine the internal structure of axisymmetric stationary jets knowing in general case five 'integrals of motion', which are energy $E(\Psi)$ and angular momentum $L(\Psi)$ flux, electric potential related to angular velocity $\Omega_{\rm F}(\Psi)$, entropy $s(\Psi)$, and the particle-to-magnetic flux ratio $\eta(\Psi)$. All these quantities have to be constant along magnetic surfaces $\Psi = {\rm const}$. In particular, it was shown that a jet with total zero electric current can exist only in the presence of the external media with finite pressure $P_{\rm ext}$. Thus, it is the ambient pressure $P_{\rm ext}$ that determines the transverse dimension of astrophysical jets.

As was shown by Beskin (1997) and Beskin & Malyshkin (2000), for cylindrical flow it is convenient to reduce one second-order Grad–Shafranov equation to two first-order ordinary differential equations for magnetic flux $\Psi(r_{\perp})$ and poloidal Alfvénic Mach number $\mathcal{M}(r_{\perp})$,

$$\mathcal{M}^2 = \frac{4\pi\mu\eta^2}{n}. \tag{4}$$

Here n is the number density in the comoving reference frame and μ is relativistic enthalpy. The first equation is the relativistic Bernoulli equation $u_{\rm p}^2 = \gamma^2 - u_{\varphi}^2 - 1$, where $u_{\rm p}$ and u_{φ} are the poloidal and toroidal components of four-velocity $\boldsymbol{u}$, respectively. Replacements for γ, $u_{\rm p}$, and u_{φ} in the Bernoulli equation lead to the form

$$\frac{\mathcal{M}^4}{64\pi^4 r_{\perp}^2}\left(\frac{{\rm d}\Psi}{{\rm d}r_{\perp}}\right)^2 = \frac{K}{r_{\perp}^2 A^2} - \mu^2\eta^2. \tag{5}$$

Here

$$A = 1 - \Omega_{\rm F}^2 r_{\perp}^2/c^2 - \mathcal{M}^2 \tag{6}$$

is the Alfvénic factor,

$$K = r_{\perp}^2 (e')^2 (A - \mathcal{M}^2) + \mathcal{M}^4 r_{\perp}^2 E^2 - \mathcal{M}^4 L^2 c^2, \tag{7}$$

and $e' = E - \Omega_{\rm F} L$. The second equation determines the Mach number $\mathcal{M}$:

$$\left[\frac{(e')^2}{\mu^2\eta^2} - 1 + \frac{\Omega_{\rm F}^2 r_{\perp}^2}{c^2} - A\frac{c_{\rm s}^2}{c^2}\right]\frac{{\rm d}\mathcal{M}^2}{{\rm d}r_{\perp}} = \frac{\mathcal{M}^6 L^2 c^2}{A r^3 \mu^2\eta^2}$$
$$+ \frac{\Omega_{\rm F}^2 r_{\perp}\mathcal{M}^2}{c^2}\left[2 - \frac{(e')^2}{A\mu^2\eta^2}\right] + \mathcal{M}^2\frac{e'}{\mu^2\eta^2}\frac{{\rm d}\Psi}{{\rm d}r_{\perp}}\frac{{\rm d}e'}{{\rm d}\Psi}$$
$$+ \frac{\mathcal{M}^2 r_{\perp}^2}{2c^2}\frac{{\rm d}\Psi}{{\rm d}r_{\perp}}\frac{{\rm d}\Omega_{\rm F}^2}{{\rm d}\Psi} - \mathcal{M}^2\left(1 - \frac{\Omega_{\rm F}^2 r_{\perp}^2}{c^2} + 2A\frac{c_{\rm s}^2}{c^2}\right)\frac{{\rm d}\Psi}{{\rm d}r_{\perp}}\frac{1}{\eta}\frac{{\rm d}\eta}{{\rm d}\Psi}$$
$$- \left[\frac{A}{n}\left(\frac{\partial P}{\partial s}\right)_n + \left(1 - \frac{\Omega_{\rm F}^2 r^2}{c^2}\right)T\right]\frac{\mathcal{M}^2}{\mu}\frac{{\rm d}\Psi}{{\rm d}r_{\perp}}\frac{{\rm d}s}{{\rm d}\Psi}. \tag{8}$$

Here T is the temperature, $c_{\rm s}$ is the sound velocity defined as $c_{\rm s}^2 = (\partial P/\partial n)|_s/m_{\rm p}$, $\mu = m_{\rm p}c^2 + c_{\rm s}^2/(\Gamma - 1)$ is again the relativistic enthalpy, $m_{\rm p}$ is the particle mass, and P is the gas pressure. As a result, Bernoulli equation (5) and equation (8) form the system of two ordinary differential equations for the Mach number $\mathcal{M}(r_{\perp})$ and the magnetic flux $\Psi(r_{\perp})$ describing cylindrical relativistic jets.

As was already stressed, the solution depends on our choice of five integrals of motion. On the other hand, it is important to note that by determining the functions $\mathcal{M}^2(r_{\perp})$ and $\Psi(r_{\perp})$ one can find the jet radius $d_{\rm jet}$ and the profile of the current $I(r_{\perp})$, the particle energy, and the toroidal component of the four-velocity from the solution of a problem under consideration. In particular, as

$$\frac{I}{2\pi} = \frac{L - \Omega_{\rm F} r_{\perp}^2 E/c^2}{1 - \Omega_{\rm F}^2 r_{\perp}^2/c^2 - \mathcal{M}^2}, \tag{9}$$

the condition of the closing of the electric current within the jet $I(\Psi_{\rm tot}) = 0$ can be rewritten as $L(\Psi_{\rm tot}) = 0$ and $\Omega_{\rm F}(\Psi_{\rm tot}) = 0$ simultaneously, where $\Psi_{\rm tot}$ is the given total magnetic flux in the jet.

For this reason we use the following expressions for these integrals:

$$L(\Psi) = \frac{\Omega_0\Psi}{4\pi^2}\sqrt{1 - \frac{\Psi}{\Psi_{\rm tot}}}, \tag{10}$$

$$\Omega_{\rm F}(\Psi) = \Omega_0\sqrt{1 - \frac{\Psi}{\Psi_{\rm tot}}}. \tag{11}$$

In the vicinity of a rotation axis these integrals correspond to well-known analytical force-free solution for homogeneous poloidal magnetic field (see Beskin 2010 for more detail). On the other hand, they both vanish at the jet boundary that guarantees the fulfilment of the condition $I(\Psi_{\rm tot}) = 0$.

Here we want to stress the novel point in our this work. We recall that careful matching of a solution inside the jet with the external media was produced only recently. The difficulty in doing the matching is due to very low energy density of the external media in comparison with the energy density inside the relativistic jet. For this reason, in most cases the infinitely thin current sheet was introduced at the jet boundary. Moreover, the external pressure was very often modelled by homogeneous magnetic field $B_{\rm ext}^2/8\pi = P_{\rm ext}$.

In contrast, Beskin et al. (2017) presented an approach that is free of the difficulties mentioned above. Following this paper we consider relativistic jet submerged into unmagnetized external media with finite gas pressure $P_{\rm ext}$. Neither external magnetic field nor infinitely thin current sheet are assumed. We succeed in doing so due to the boundary conditions (10) and (11) at the jet boundary $r_\perp = d_{\rm jet}$.

In addition, we assume that both magnetic field and flow velocity vanish at the jet boundary $r_\perp = d_{\rm jet}$. As one can see from equation (9), our choice of $L(\Psi)$ and $\Omega_{\rm F}(\Psi)$ guarantees that toroidal component $B_\varphi \propto I/r$ vanishes at the jet boundary. One can find that the toroidal velocity u_φ also vanished at the jet boundary due to algebraic relation

$$u_\varphi = \frac{1}{\mu\eta c r}\frac{(E - \Omega_{\rm F} L)\Omega_{\rm F} r^2/c^2 - L\mathcal{M}^2}{1 - \Omega_{\rm F}^2 r^2/c^2 - \mathcal{M}^2}. \tag{12}$$

On the other hand, using relation $n\boldsymbol{u}_{\rm p} = \eta\boldsymbol{B}_{\rm p}$ one can conclude that the conditions $\boldsymbol{u}_{\rm p} = 0$ and $\boldsymbol{B}_{\rm p} = 0$ can be compatible with one another for finite n and η. For simplicity we consider here the case

$$\eta(\Psi) = \eta = {\rm const}. \tag{13}$$

In addition, we suppose that the flow remains supersonic up to the very boundary: $\mathcal{M}(d_{\rm jet}) > 1$. This supposition allows us to simplify our consideration. Indeed, in this case equation (8) has no additional singularity at the Alfvénic surface $A = 0$ in the vicinity of the jet boundary. Finally, in what follows we put

$$s(\Psi) = s = {\rm const}. \tag{14}$$

This non-zero value allows us to match magnetically dominated flow to the external media with finite pressure. As was shown by Beskin et al. (2017), thermal effects play important role only in the very vicinity of the jet edge, while the main properties of the jet depend on the ambient pressure $P_{\rm ext}$ (the value of s determines the width of the boundary layer).

Finally, energy integral $E(\Psi)$ is expressed as (Beskin & Okamoto 2000)

$$E(\Psi) = \Omega_{\rm F} L + \mu_0\eta\gamma(\Psi). \tag{15}$$

Here $\gamma(\Psi)$ is the Lorentz factor at the base of the jet, and $\gamma(0) = \gamma_{\rm in}$ is the Lorenz factor on the jet axis. We require that $\gamma(\Psi_{\rm tot}) = 1$ meaning that the velocity vanishes at the jet boundary. Below for simplicity we chose the radial profile of the injection Lorentz factor as

$$\gamma(\Psi) = \gamma_{\rm in} - (\gamma_{\rm in} - 1)\frac{\Psi}{\Psi_{\rm tot}}. \tag{16}$$

In addition to five integrals of motion, the systems (5) and (8) require two boundary conditions. The first one is the clear condition at the symmetry axis,

$$\Psi(0) = 0. \tag{17}$$

As to the second one, it can be found from the pressure balance at the jet boundary,

$$P(d_{\rm jet}) = P_{\rm ext}. \tag{18}$$

This procedure fully determines the solution of the problems (5), (8), and (17)–(18), and ensures its uniqueness. For each ambient pressure $P_{\rm ext}$ the obtained solution is a cross-cut profile at z = const. Piling of the different cross-cuts is a solution for an outflow in which one may neglect the derivatives in z in comparison with the derivatives in $r_\perp$ in the two-dimensional Grad–Shafranov and Bernoulli equations. This can be done for highly collimated, at least as a parabola, outflows (Nokhrina et al. 2015).

We apply here cylindrical approximation to a conical jet with small opening angle. As $v_\varphi \ll v_z$ and $v_r \ll v_z$, one has to consider all components of velocity. We assume that jet has conical form with half-opening angle $\theta \approx 2.5^\circ$. It gives

$$u_z(r_\perp) = u_{\rm p}\cos\left(\frac{r_\perp}{d_{\rm jet}}\theta\right), \tag{19}$$

$$u_r(r_\perp) = u_{\rm p}\sin\left(\frac{r_\perp}{d_{\rm jet}}\theta\right). \tag{20}$$

These formulae are to be valid also in the case of parabolic jet where θ is an angle between tangent and z-axis at the cross-cut. An important formula for calculations of the Doppler boosting factor is for the angle between velocity of plasma parcel and the line-of-sight χ. Introducing Cartesian coordinate system such that $\varphi = 0$ corresponds to x-direction and $\varphi = \pi/2$ corresponds to the y-direction, one obtains for line-of-sight vector

$$\boldsymbol{e} = (\sin\alpha, 0, \cos\alpha), \tag{21}$$

where α is an angle between the jet axis z and the line of sight. Hence,

$$\cos\chi = \frac{(v_\varphi\sin\varphi + v_r\cos\varphi)\sin\alpha + v_z\cos\alpha}{\sqrt{v_{\rm p}^2 + v_\varphi^2}}. \tag{22}$$

2.1 Internal structure of relativistic jets

As was already stressed, for given five 'integrals of motion' the solution at each cross-section is fully determined by the value of the ambient pressure $P_{\rm ext}$. It concerns the jet width $d_{\rm jet}$ as well. For this reason in what follows we use the jet thickness $d_{\rm jet}$ as a main parameter as it can be directly determined from observations.

On the other hand, as was shown by Beskin et al. (2017), our choice of 'integrals of motion' allows us to express them through only one dimensionless quantity:

$$\sigma_{\rm M} = \frac{\Omega_0^2\Psi_{\rm tot}}{8\pi^2\mu\eta c^2}, \tag{23}$$

i.e. through the Michel magnetization parameter, which is the parameter of a 'central engine' (it gives the maximum bulk Lorentz factor of the outflow). In addition, we use parameters of M87 black hole for calculations below. Another assumption is the value of the regular magnetic field nearby the event horizon $B = 10^4$ G. It is also assumed that magnetization parameter $\sigma_{\rm M} = 10$–100. This choice is reasonable for AGNs (see e.g. Nokhrina et al. 2015).

The profiles of magnetic field components, velocities of particles, number density, and Lorentz factor of plasma are presented in Figs 1–5 for two different width of the jet $d_{\rm jet}$ and two different values of magnetization parameter $\sigma_{\rm M}$. As we show in Fig. 1, our choice of integrals of motion results in fast decrease of the number density in laboratory frame $n_{\rm e} = n\gamma$ with the distance from the rotation axis, where n is found via equation (4). As was mentioned above, number density is determined by magnetization parameter $\sigma_{\rm M}$. As we see, number density is larger for smaller $\sigma_{\rm M}$. The dramatic growth of the density at the jet boundary is just dictated by pressure balance inside the thin boundary layer (Beskin et al. 2017),

$$P + \frac{B^2}{8\pi} = {\rm const}, \tag{24}$$

and by vanishing magnetic field outside the jet. Inside the jet the 'cavity' is supported by large magnetic field pressure and by centrifugal force.

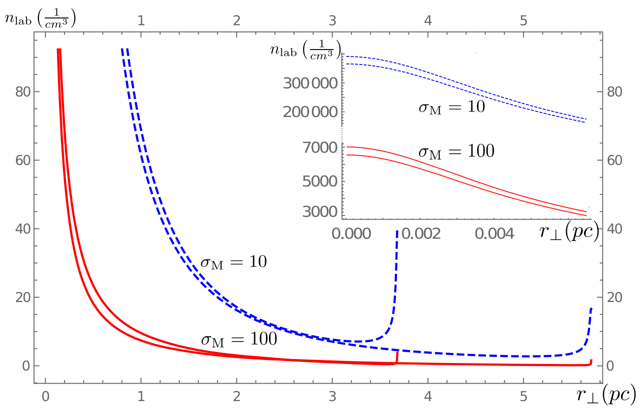

Figure 1. Number density profiles at two different cross-section of the jet in the laboratory frame. Red solid lines correspond to magnetization parameter $\sigma_{\rm M} = 100$, and dashed blue lines to $\sigma_{\rm M} = 10$. The region of high densities at the axis of the jet is zoomed in.

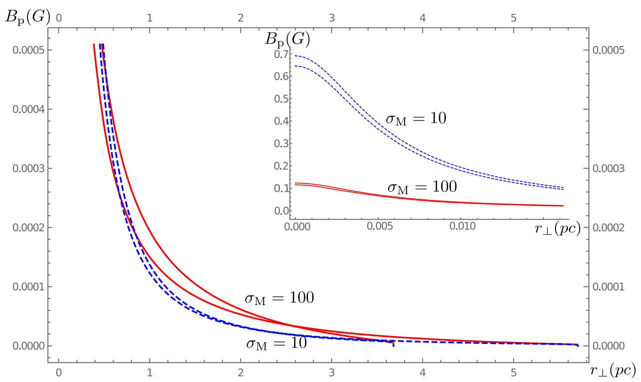

Figure 2. Poloidal magnetic field at two different cross-sections of the jet. Red solid lines correspond to magnetization parameter $\sigma_{\rm M} = 100$, and dashed blue lines to $\sigma_{\rm M} = 10$. The central region is resolved.

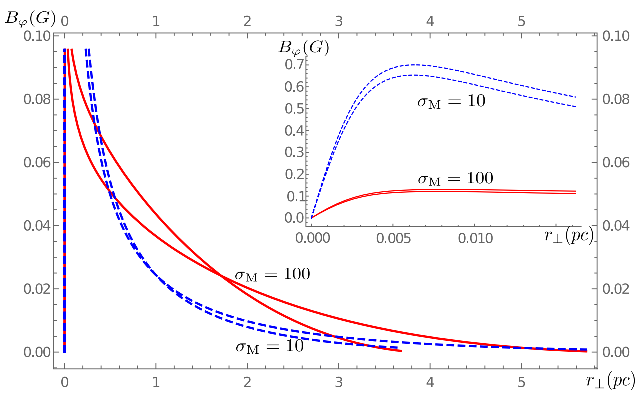

Figure 3. Toroidal component of magnetic fields at two different cross-sections of the jet. Red solid lines correspond to magnetization parameter $\sigma_{\rm M} = 100$, and dashed blue ones to $\sigma_{\rm M} = 10$. The central region is resolved.

3 RESULTS

Further, in Figs 2 and 3 we show the structure of magnetic field inside the jet. As we see, the magnetic field also forms the central core and then drops towards the jet boundary. In the narrow central part the toroidal component growth linearly as $B_\varphi \propto I/r$ and $I = \pi j_{\rm p} r^2$. Here $j_{\rm p}$ is the current density. Outside the light cylinder $R_{\rm L}$ toroidal magnetic field prevails up to the very edge $B_\varphi \gg B_{\rm p}$. Since the jet radius in quasi-cylindrical part is $d_{\rm jet} \approx 10^2$–$10^4 R_{\rm L}$, the relative size of region $B_\varphi < B_{\rm p}$ is extremely small.

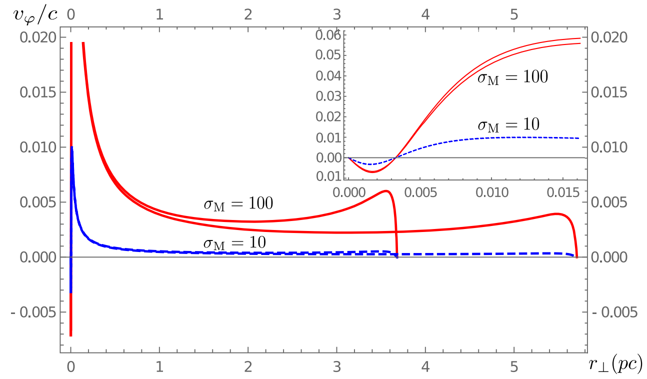

Figure 4. Toroidal components of hydrodynamical velocities at two different cross-sections of the jet. Plasma changes its rotational direction in the innermost region. Red solid lines correspond to magnetization parameter $\sigma_{\rm M} = 100$, and dashed blue lines to $\sigma_{\rm M} = 10$. The central region of peak velocity is resolved.

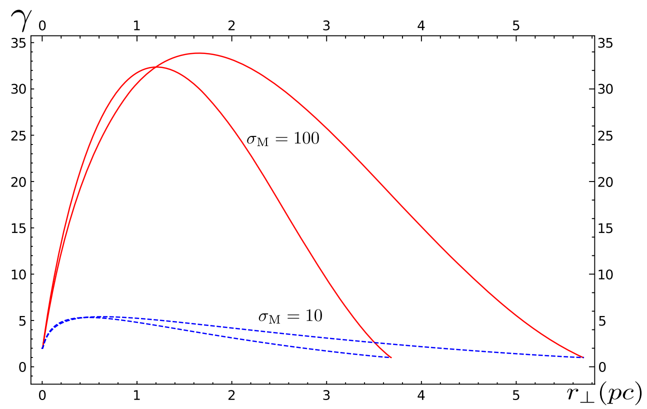

Figure 5. Profiles of the Lorentz factors at two different cross-sections of the jet. Red solid lines correspond to magnetization $\sigma_{\rm M} = 100$, and dashed blue lines correspond to $\sigma_{\rm M} = 10$. Lorentz factor at the axis $\gamma_{\rm in} = 2$.

Besides, in Fig. 4 we show the toroidal components of hydrodynamical velocity v_φ. The differences in the magnitude are attributed to the particle-to-magnetic flux ratio that is larger for smaller magnetization parameter (23). In any way, maximum value for toroidal velocity v_φ cannot exceed a few tenths of speed of light c. In this sense our predictions do not contradict observational data (Mertens et al. 2016). On the other hand, as one can see directly from equation (12), toroidal velocity v_φ can hardly be determined theoretically. The point is that two terms in the numerator have the same order of magnitude, the first one being related to the sliding along the magnetic surface, and the second one being related to the angular momentum. For example, for monopole magnetic field (and for slow rotation) the toroidal velocity vanishes (Bogovalov 1992; Beskin & Okamoto 2000). For this reason it is not surprising that v_φ can change sign.

Finally, as is shown in Fig. 5, the magnitude of the Lorentz factor is also determined by magnetization parameter, its value being larger for wider jet (and, certainly, for larger magnetization parameter $\sigma_{\rm M}$). This fact is the illustration of the well-known dependence (1).

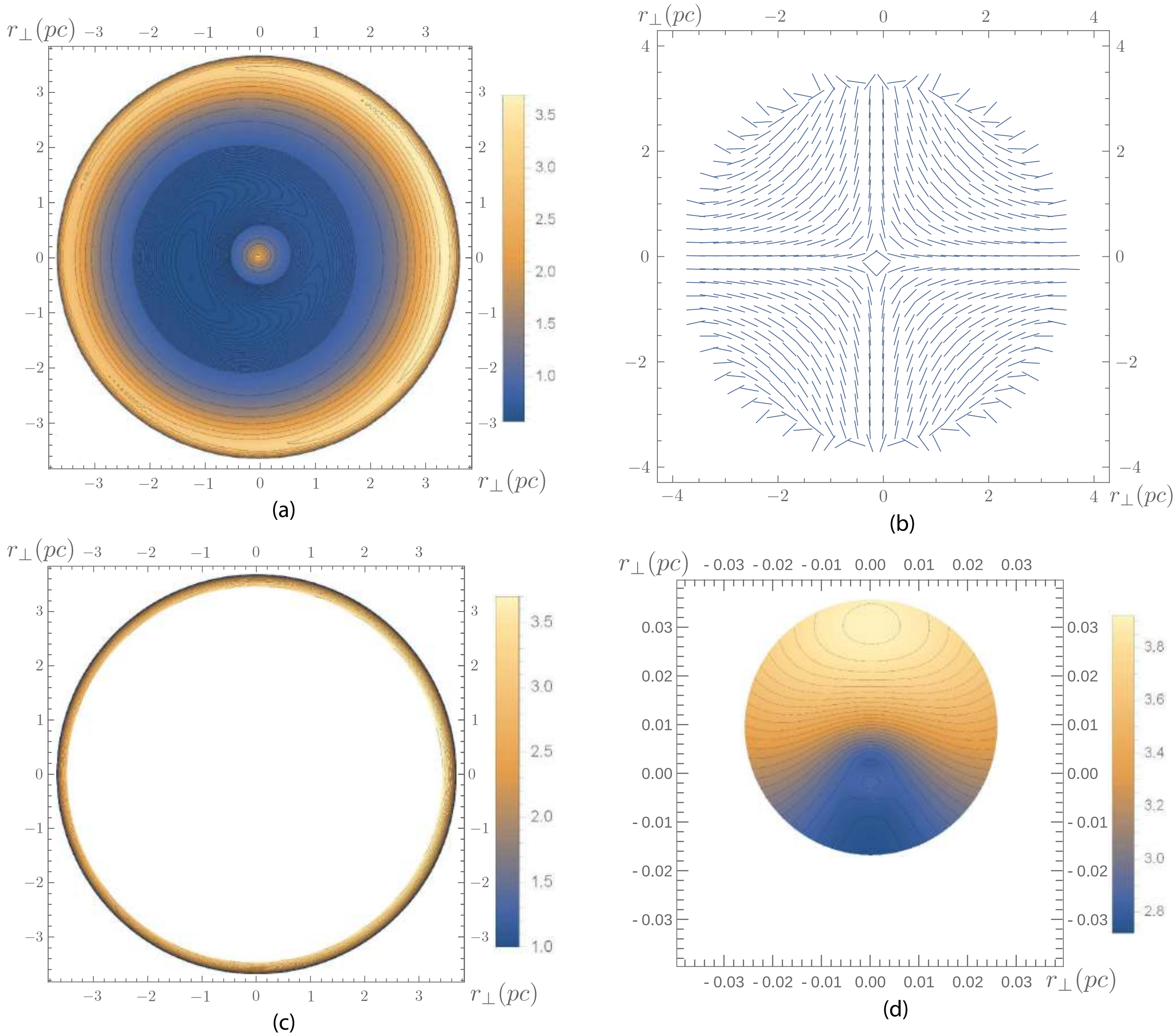

Figure 6. The distribution of the Doppler factor on the cross-section of the jet for inclination angle $\alpha = 18^\circ$ for parameters of M87 and $\sigma_{\rm M} = 100$, $\gamma_{\rm in} = 2$ as would be seen by an observer looking down on the jet from the above and from the right at an angle $\alpha = 18^\circ$ with respect to the jet axis. (a) Map of Doppler boosting factor as a whole. Contour lines are drawn with a step 0.01 for $\delta \in (0, 0.8)$ and 0.3 for $\delta \in (0.8, 4)$. (b) Map of the directions of electric vector of linearly polarized radio emission. (c) Map of radiation that is not depressed by relativistic beaming effect. (d) Zoom in on the central region of the map (c) that is not resolved on plot (c).

Indeed, it can be seen that in the central part of the jet Lorentz factor grows linearly as our choice of 'integrals of motion' coincides with the force-free choice in the vicinity of the axis.

It is also necessary to stress that there is no acceleration of particles along the rotational axis because the flux of electromagnetic energy $E \propto \Omega_{\rm F} I$ is equal to zero there and Lorentz factor at the axis is chosen $\gamma_{\rm in} = 2$. The Lorentz factor also does not change at the boundary because I is zero there too. In contrast, the Lorenz factor intensively changes at middle radii where according to equation (16) the magnetization is initially high.

3.1 Doppler maps

The maps of the Doppler factor δ (3) are presented in Figs 6–10 for different inclination angles α and for different magnetization parameters $\sigma_{\rm M}$. Comparing now the Lorentz factor distribution with the Doppler maps one can conclude that for large enough α radiation from the regions with highest Lorentz factor cannot be detected. These components may be seen in BL Lac objects only.

Indeed, the constraints on the visible part of a jet are governed by relativistic beaming effect. If an angle χ between line of sight and velocity of plasma is greater than $1/\gamma$, radiation cannot be detected. As a result, as shown in Fig. 6(c), observer can see only the regions with small enough γ, i.e. outer parts of a jet and the jets core. For example, for M87 (the black hole mass $M = 3 \times 10^9$ M$_\odot$, $a = 0.1$, distance 17 Mpc, and inclination angle $\alpha = 18^\circ$) the angular size of central bright core is $\sim 10^{-1}$ mas, while the peak angular resolution of VLBI is 1 mas for M87 at distance 10–100 mas from the central engine at frequency 15 GHz (Kovalev, personal communication).

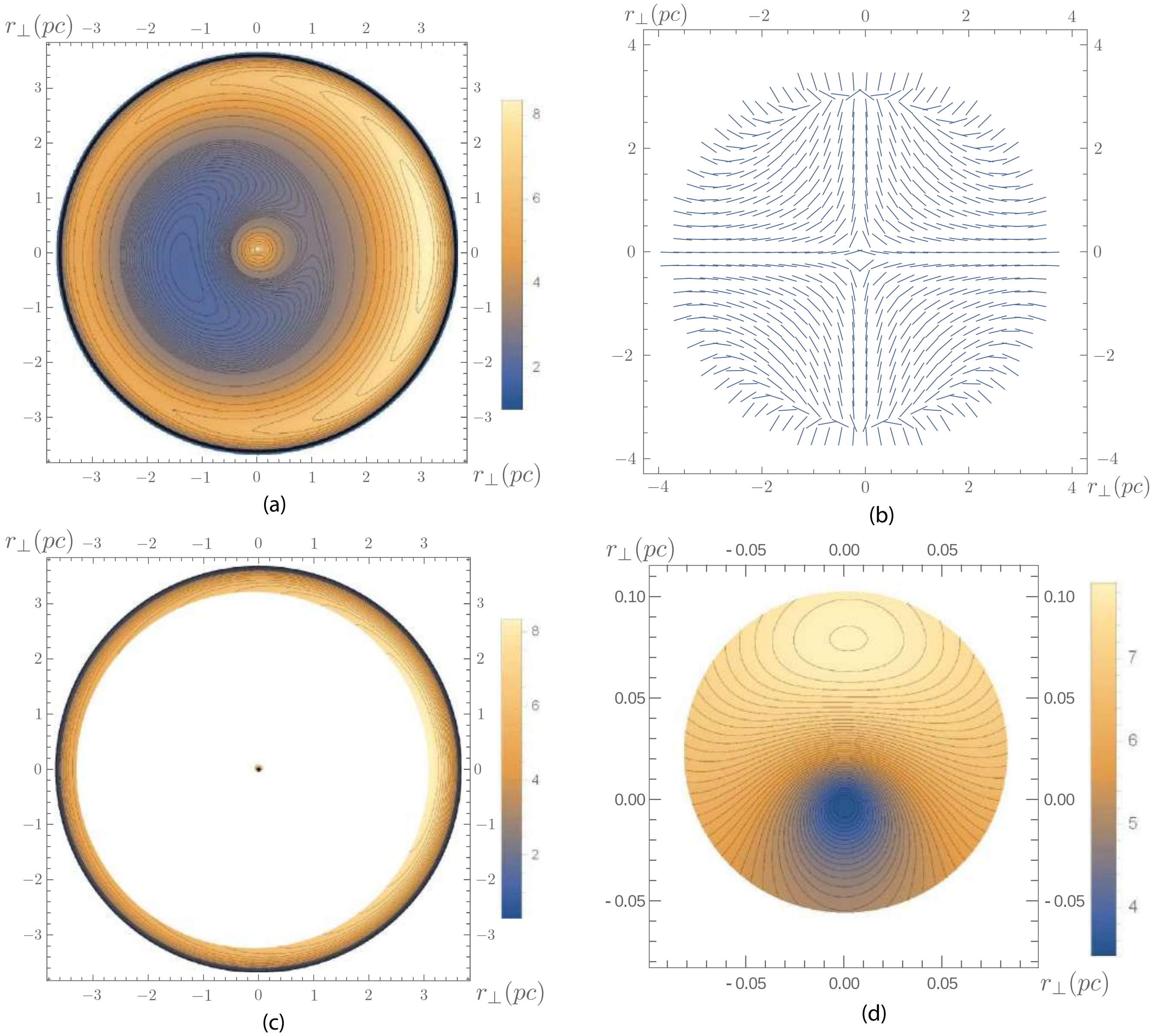

Figure 7. The same as at Fig. 6, but for inclination angle $\alpha = 9^{\circ}$. Magnetization parameter $\sigma_{\rm M} = 100$. Contour lines are drawn with step 0.05 for $\delta \in (0, 3)$ and 0.3 for $\delta \in (3, 8)$.

Nevertheless, the core can be resolved with VLBI if the jet is less magnetized, e.g., for Michel magnetization parameter $\sigma_{\rm M} = 10$ (see Fig. 9).

We also present the results for the distributions of the Doppler factor in the case of fixed angle between rotational axis of the jet and the line-of-sight $\alpha = 18^{\circ}$ (as for the jet in M87) and different magnetization parameters $\sigma_{\rm M} = (10, 30)$. The value $\sigma_{\rm M} = 100$ was considered earlier. Larger values $\sigma_{\rm M} > 100$ look unreasonable because only the radiation from the very narrow ring at the jet boundary could be detected for large $\sigma_{\rm M}$, which does not match the observations of more wider structures across the M87 jet.

As was shown above, outer annular region of a jet has both low plasma density and low magnetic field pressure. Hence, radiation from this region is to be double depressed. The map of luminosity distribution will be presented in the future papers. Here for simplicity we consider everywhere the solutions with the same radius $r_{\rm jet} =$ 3.7 pc corresponding to ambient pressure $P_{\rm ext} \approx 10^{-10}$ dyn cm^{-2} for $\sigma_{\rm M} = 100$ and to $P_{\rm ext} \approx 10^{-9}$ dyn cm^{-2} for $\sigma_{\rm M} = 10$ (see fig. 5 in Beskin et al. 2017).

Finally, we discuss the polarization properties of radio emission, which do not depend on the number density of radiating particles. Indeed, relativistic motion of emitting plasma also affects the direction of observed linear polarization of synchrotron radiation that properties in the rest frame of plasma (where only ordered magnetic field $\boldsymbol{B}'$ is present and electric field $\boldsymbol{E}'$ vanishes) are well known (see e.g. chap. 5 in Ginzburg 1989). Specifically, for highly relativistic radiating particles the electric field $\boldsymbol{e}'$ of the wave is perpendicular to the local direction of the static magnetic field $\boldsymbol{B}'$.

The changes in polarization properties of polarized electromagnetic wave under Lorentz transformations were first mentioned and applied in astrophysical settings by Cocke & Holm (1972). After

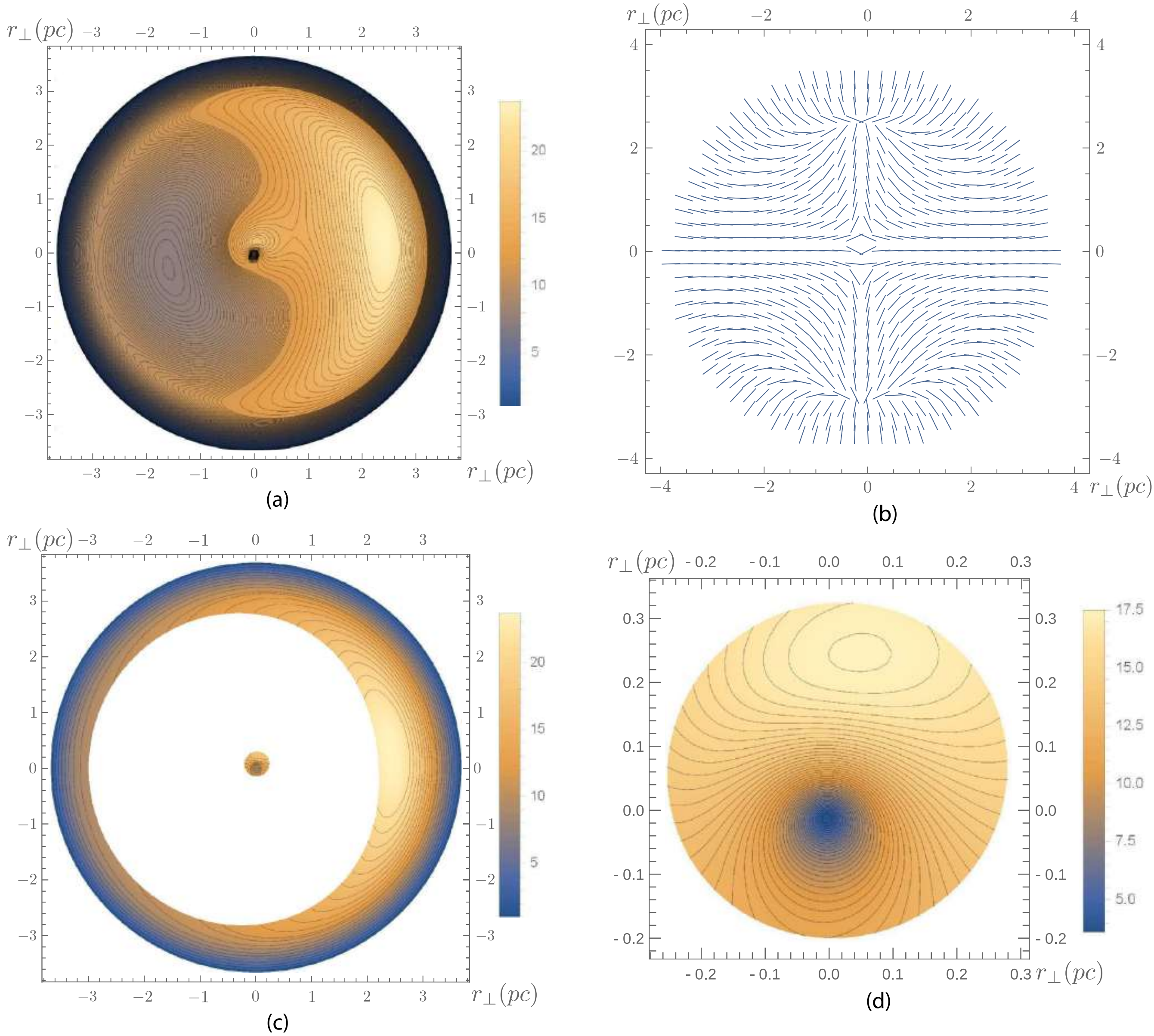

Figure 8. The same as at Fig. 6, but for inclination angle $\alpha = 4^{\circ}$. Magnetization parameter $\sigma_{\mathrm{M}} = 100$. Contour lines are drawn with step 0.1 for $\delta \in (0, 11.5)$ and 0.5 for $\delta \in (11.5, 20)$.

Lorentz boost the observed direction of the wave electric vector in observer's reference frame is, in general, not perpendicular to the direction of the magnetic field. Calculations of polarization properties of synchrotron radiation emitted by relativistic extragalactic jets were done by many authors (see e.g. Blandford & Königl 1979; Pariev et al. 2003; Lyutikov et al. 2005; Peirson & Romani 2018). However, two-dimensional distribution of polarization over cross-section of the jets was not included into consideration in these works.

Here we calculate and draw maps of unit vector $\hat{\boldsymbol{e}}$ along the wave electric field $\boldsymbol{e}$ in linearly polarized synchrotron radiation as seen by the observer. Each small patch of plasma contains isotropically distributed relativistic particles with energy spectrum $\mathrm{d}N = K\epsilon^{-p}\mathrm{d}\epsilon$. We do not consider circular polarization at the moment. This approximation corresponds to ultrarelativistic energies of emitting particles. Then, the degree of linear polarization emitted by every small patch of the jets is $\Pi_0 = (p + 1)/(p + 7/3)$ (Ginzburg 1989). Under vacuum approximation the observed radiation is obtained by integration of Stokes parameters of independent incoherent emitters over the line of sight. Because each emitter has varying direction of the magnetic field and varying relativistic velocities, the direction of polarization $\hat{\boldsymbol{e}}$ for each emitter also varies. As a result, the degree of polarization in the total integrated radiation flux along each line of sigh will be smaller than the upper limit Π_0.

Here we leave the construction of integrated observable maps of synchrotron radiation (including consideration of propagation effects in thermal plasma, such as Faraday rotation, as well as self-absorption effects) for forthcoming series of works. Below we restrict ourselves only to the construction of polarization maps that

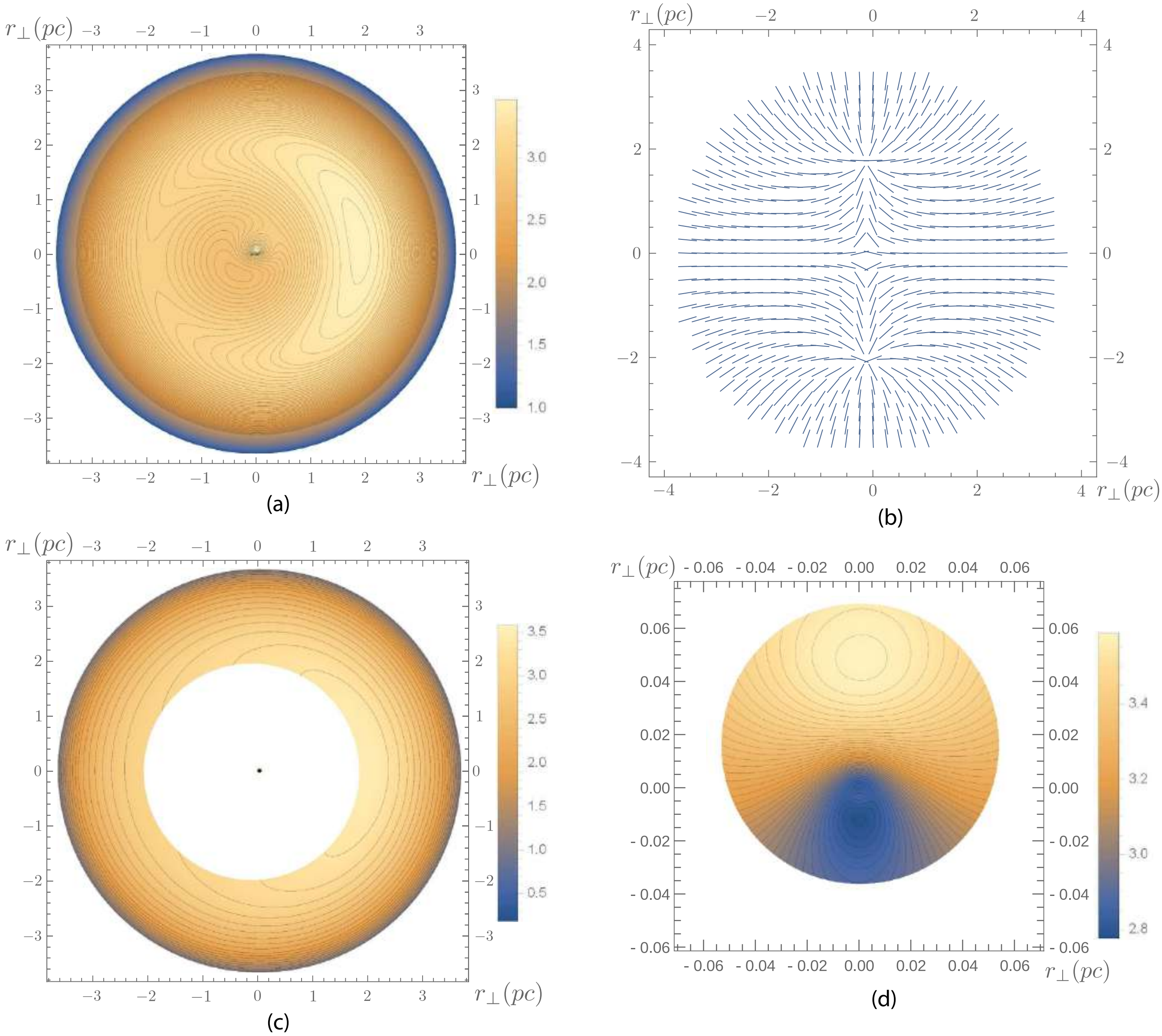

Figure 9. The same as at Fig. 6, but for inclination angle $\alpha = 18^{\circ}$ and magnetization parameter $\sigma_{\rm M} = 10$. Contour lines are drawn with step 0.01 for $\delta \in (0, 2)$ and step 0.1 for $\delta \in (2, 4)$.

correspond to individual cross-sections of a jet for given distance from the 'central engine'.

General expressions giving the polarization unit vector $\hat{\boldsymbol{e}}$ in terms of the observed direction of magnetic field at the emitter, unit vector $\hat{\boldsymbol{B}}$, direction of the wave vector of the wave to the observer, unit vector $\boldsymbol{n}$, and the velocity $\boldsymbol{v}$ of the emitter were derived in compact form in Lyutikov, Pariev & Blandford (2003), formula (C5) in appendix C there. We reproduce these expressions here for convenience and keep speed of light c in line with the notations used in this work:

$$\hat{\boldsymbol{e}} = \frac{\boldsymbol{n} \times \boldsymbol{q}}{\sqrt{q^2 - (\boldsymbol{n} \cdot \boldsymbol{q})^2}}, \quad \boldsymbol{q} = \hat{\boldsymbol{B}} + \boldsymbol{n} \times (\boldsymbol{v} \times \hat{\boldsymbol{B}})/c. \tag{25}$$

Directions of polarization vector $\hat{\boldsymbol{e}}$ are plotted in Figs 6–10 in panels (b). As we see, linear polarization has a rather complicated structure, which should be taken into account when analysing observations. In the observer's frame the magnetic field is dominated by the toroidal component for all radii, therefore, vectors $\hat{\boldsymbol{e}}$ would be directed radially everywhere on the map if the bulk motion is non-relativistic. In reality the flow is non-relativistic only in the vicinity of the outer boundary of the jet, because at the boundary itself all components of velocity vanish. Accordingly, we observe the ring of radially directed polarization vectors near the outer edge of the jet in panels (b) in Figs 6–10. Inside the ring the swing of the polarization direction due to the relativistic aberration becomes significant when $\gamma(r)\alpha \geq 1$. Because γ decreases toward the jet boundary, the size of the ring with radially directed polarization vectors $\hat{\boldsymbol{e}}$ is smaller for larger α and is also smaller for faster flows with larger γ and larger $\sigma_{\rm M}$.

4 DISCUSSION AND CONCLUSION

In this paper, we investigated the internal structure of relativistic jets and their influence on the polarization properties of the observed

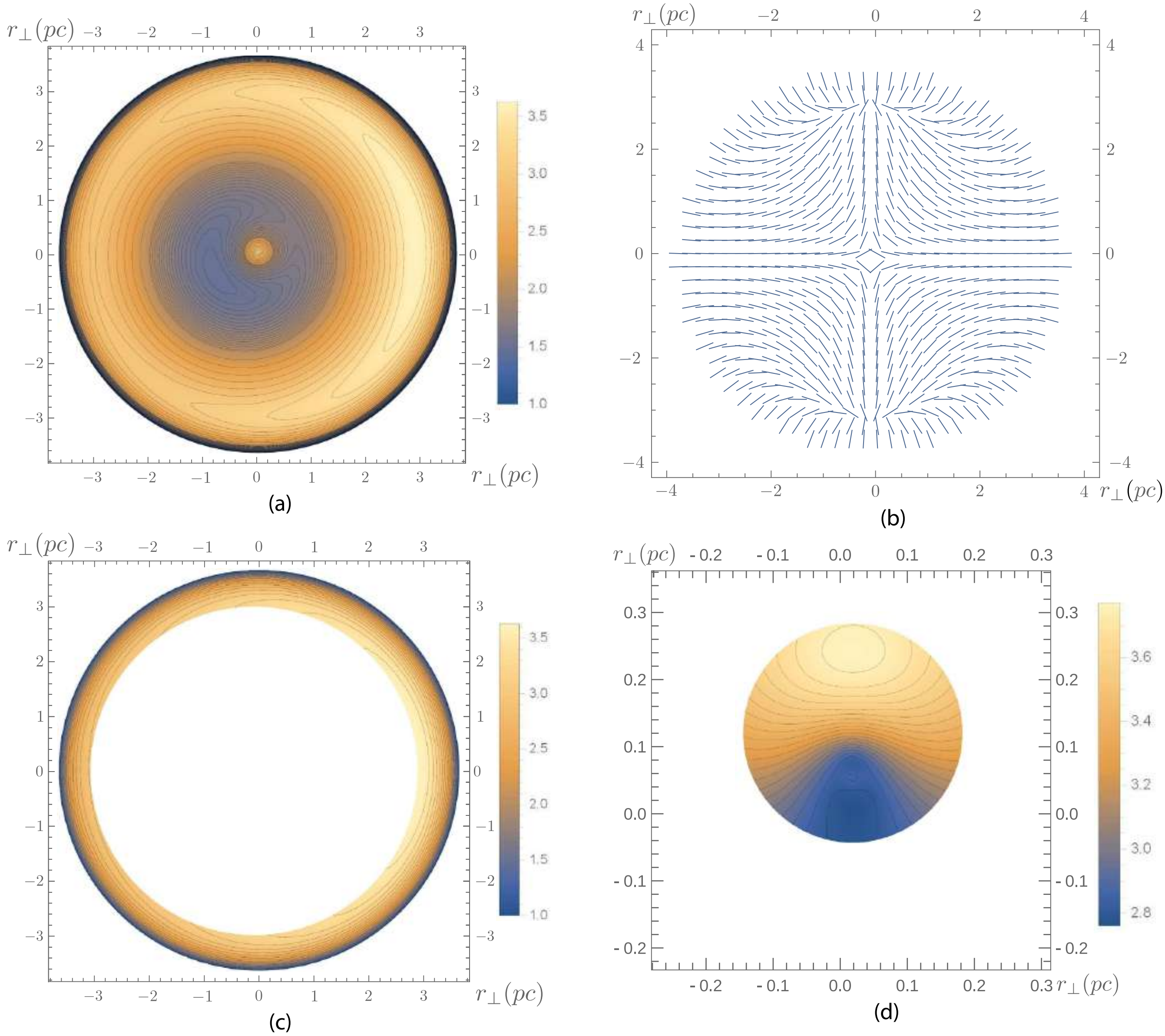

Figure 10. The same as at Fig. 6, but for inclination angle $\alpha = 18^\circ$ and magnetization parameter $\sigma_{\rm M} = 30$. Contour lines are drawn with step 0.01 for $\delta \in (0, 0.8)$ and 0.3 for $\delta \in (0.8, 4)$.

radiation. In particular, the profiles of magnetic field, velocity, and number density across cylindrical jet submerged into non-magnetized gas at rest were determined. Another result is the map of the Doppler boosting factor at the cross-section of the jet together with the map of relativistic beaming effect under consideration.

It is shown how both the magnetic field and the number density gradually drop to external medium values close to the external boundary of the jet. We demonstrated that regardless the inclination angle α between the jet axis and the line of sight, only outer ring and central core can be observed. The size of central core is very small and can be measured only when the angle between the jet axis and the line of sight is small.

It is necessary to notice that the central core must exist for MHD mechanism of acceleration since the electromagnetic energy flux $\sim\Omega_{\rm F} I$ at the rotation axis is zero, and Lorentz factor is conserved along the axis. The outer part may be relatively large with dramatic change of Doppler factor across the ring, but the outer part is supposed to be dim.

The multiplicity parameter calculated using results of our model is

$$\lambda = \frac{n^{(\rm lab)}}{n_{\rm GJ}} \approx 5 \times 10^{12}, \qquad (26)$$

where $n_{\rm GJ} = \Omega_{\rm F} B_{\rm p}/(2\pi c e)$ is Goldreich–Julian density, which is the number density of charged particles just enough to screen the longitudinal electric field. This result is in agreement with observations because $\lambda\sigma_{\rm M} \approx (W_{\rm tot}/W_{\rm a})^{1/2}$, where $W_{\rm tot}$ is the total energy losses of the jet, and $W_{\rm a} = m_{\rm e}^2 c^5/e^2 \approx 10^{17}\ {\rm erg\,s^{-1}}$ (see Beskin 2010 for more detail). It gives $\lambda\sigma_{\rm M} \sim 10^{14}$, which agrees with equation (26) for $\sigma_{\rm M}$ from 10 to 100.

In addition, it is shown that the size of the central core actually does not depend on Michel magnetization parameter $\sigma_{\rm M}$ but is a function of the inclination angle α. In contrast, the size of the outer ring depends on both σ_M and the angle α: the lower each value, the wider the ring. The most reasonable Michel parameter to explain observations of M87 is $\sigma_M \approx 10$. This value of σ_M is able to reproduce simultaneously the size of the outer bright core, bulk Lorentz factor $\gamma \approx 6$, the observation of superluminal motion, and numerical simulations (see e.g. Porth et al. 2011). We have also calculated observed directions of linear polarization of synchrotron radiation emitted by cross-sectional layers of the jet. The effect of relativistic aberration on polarization was also taken into account. This effect and obtained distributions of polarization direction are fundamental basics of understanding and interpreting present and future VLBI polarization measurements of relativistic magnetized jets. Full integrated radio images of the jet together with its rotation measure and polarization will be presented in the following papers.

ACKNOWLEDGEMENTS

We thank Y. N. Istomin, S. V. Chernov, and E. E. Nokhrina for useful discussions, and especially 14th School of Modern Astrophysics SOMA-2018 (http://astrosoma.ru) for provision of fruitful ideas and discussions. This work was supported by Russian Foundation for Basic Research (Grant No. 17-02-00788).

REFERENCES

Ardavan H., 1976, ApJ, 204, 889
Beskin V. S., 1997, Phys. Uspekhi, 40, 659
Beskin V. S., 2010, MHD Flows in Compact Astrophysical Objects: Accretion, Winds and Jets. Springer-Verlag, Berlin
Beskin V. S., Malyshkin L. M., 2000, Astron. Lett., 26, 208
Beskin V. S., Nokhrina E. E., 2006, MNRAS, 367, 375
Beskin V. S., Nokhrina E. E., 2009, MNRAS, 397, 1486
Beskin V. S., Okamoto I., 2000, MNRAS, 313, 445
Beskin V., Chernoglazov A., Kiselev A., Nokhrina E., 2017, MNRAS, 472, 3971
Blandford R. D., Königl A., 1979, ApJ, 232, 34
Bogovalov S. V., 1992, Soviet Astron. Lett., 18, 337
Cocke W. J., Holm D. A., 1972, Nat. Phys. Sci., 240, 161
Fendt C., Porth O., Sheikhnezami S., 2014, Int. J. Modern Physics: Conf. Ser., 28, 1460190
Ginzburg V. L., 1989, Applications of Electrodynamics in Theoretical Physics and Astrophysics. Gordon & Breach, New York
Gourgouliatos K. N., Fendt C., Clausen-Brown E., Lyutikov M., 2012, MNRAS, 419, 3048
Kim J., Balsara D. S., Lyutikov M., Komissarov S. S., 2017, MNRAS, 467, 4647
Kim J., Balsara D. S., Lyutikov M., Komissarov S. S., 2018, MNRAS, 474, 3954
Komissarov S. S., Barkov M. V., Vlahakis N., Königl A., 2007, MNRAS, 380, 51
Lery T., Heyvaerts J., Appl S., Norman C. A., 1999, A&A, 347, 1055
Lundquist S., 1950, Arkiv Fysik, 2, 361
Lyubarsky Y., 2009, ApJ, 698, 1570
Lyutikov M., Pariev V. I., Blandford R. D., 2003, ApJ, 597, 998
Lyutikov M., Pariev V. I., Gabuzda D. C., 2005, MNRAS, 360, 869
McKinney J. C., 2006, MNRAS, 368, 1561
McKinney J. C., Tchekhovskoy A., Blandford R. D., 2012, MNRAS, 423, 3083
Martí J.-M., 2015, MNRAS, 452, 3106
Mertens F., Lobanov A. P., Walker R. C., Hardee P. E., 2016, A&A, 595, A54
Nokhrina E. E., Beskin V. S., Kovalev Y. Y., Zheltoukhov A. A., 2015, MNRAS, 447, 2726
Pariev V. I., Istomin Y. N., Beresnyak A. R., 2003, A&A, 403, 805
Peirson A. L., Romani R. W., 2018, ApJ, 864, 140
Porth O., Fendt C., Meliani Z., Vaidya B., 2011, ApJ, 737, 42
Potter W. J., Cotter G., 2015, MNRAS, 453, 4070
Pushkarev A. B., Kovalev Y. Y., Lister M. L., Savolainen T., 2017, MNRAS, 468, 4992
Tchekhovskoy A., Narayan R., McKinney J. C., 2011, MNRAS, 418, L79
Vlahakis N., Königl A., 2003, ApJ, 596, 1080

This paper has been typeset from a TEX/LATEX file prepared by the author.